Taylor & Francis
Taylor & Francis Group

AEROSOL
SCIENCE
AND TECHNOLOGY

Comparison of three essential sub-micrometer aerosol measurements: mass, size and shape

Journal:	*Aerosol Science & Technology*
Manuscript ID	AST-MS-2020-015.R1
Manuscript Type:	Original Manuscript
Date Submitted by the Author:	07-Apr-2020
Complete List of Authors:	Yao, Qi; University of Maryland at College Park, Department of Chemical and Biomolecular Engineering Asa-Awuku, Akua; University of Maryland at College Park, Department of Chemical and Biomolecular Engineering; University of Maryland at College Park, Department of Chemistry and Biochemistry Zangmeister, Christopher; National Institute of Standards and Technology, Material Measurement Laboratory Radney, James; National Institute of Standards and Technology, Material Measurement Laboratory
Keywords:	differential mobility analyzer (DMA), aerosol particle mass analyzer (APM), aerodynamic aerosol classifier (AAC), mass, size, dynamic shape factor

Comparison of three essential sub-micrometer aerosol measurements: mass, size and shape

Qi Yao[a] (https://orcid.org/0000-0002-8666-2421),

Akua Asa-Awuku[a,b] (https://orcid.org/0000-0002-0354-8368),

Christopher D. Zangmeister[c] (https://orcid.org/0000-0002-6026-9293) &

James G. Radney[c*] (https://orcid.org/0000-0001-7324-8769)

[a] Department of Chemical and Biomolecular Engineering, University of Maryland, College Park, MD 20742 USA

[b] Department of Chemistry and Biochemistry, University of Maryland, College Park, MD 20742 USA

[c] Material Measurement Laboratory, National Institute of Standards and Technology, Gaithersburg, MD 20899 USA

*Corresponding author: James Radney, james.radney@nist.gov, Material Measurement Laboratory, National Institute of Standards and Technology, 100 Bureau Dr. MS 8320, Gaithersburg, MD 20899 USA.

Abstract

An instrumental trifecta now exists for aerosol separation and classification by aerodynamic diameter (D_{ae}), mobility diameter (D_m) and mass (m) utilizing an aerodynamic aerosol classifier (AAC), differential mobility analyzer (DMA) and aerosol particle mass analyzer (APM), respectively. In principle, any combination of two measurements yields the third. These quantities also allow for the derivation of the particle effective density (ρ_{eff}) and dynamic shape factor (χ). Measured and/or derived deviations between tandem measurements are dependent upon the configuration but are generally less than 10 %. Notably, non-physical values of χ (< 1) and ρ_{eff} (> bulk) were determined by the AAC-APM. Harmonization of the results requires the use of χ in the determination of m and D_m from the AAC-DMA and AAC-APM requiring either *a priori* assumptions or determination from another method. Further errors can arise from assuming instead of measuring physical conditions – e.g. temperature and pressure affect the gas viscosity, mean free path and the Cunningham slip correction factor therefore impacting D_m, D_{ae} – but are expected to have a smaller impact than χ. Utilizing this triplet of instrumentation in combination allows for quantitative determination of χ and the particle density (ρ_p). If the bulk density is known or assumed, then the packing density can be determined. The χ and ρ_p were determined to be 1.10 ± 0.03 and (1.00 ± 0.02) g cm^{-3}, respectively, for a water stabilized black

carbon mimic that resembles aged (collapsed) soot in the atmosphere. Assuming ρ_{bulk} = 1.8 g cm^{-3}, a packing density of 0.55 ± 0.02 is obtained.

1. Introduction

Physical and morphological properties (size, effective density and shape factor) and the number density of particles are required to predict aerosol behavior. Measuring these parameters accurately at the sub-micrometer level poses many challenges and several methods currently exist to quantify these properties. Most investigations use a differential mobility analyzer (DMA) – first demonstrated in 1975 (Knutson and Whitby 1975) to classify particles based upon their mobility diameter (D_m); i.e. the measured diameter that has the equivalent mobility of a spherical particle with a single net charge ($q = \pm 1$) in an electric field. The invention and development of the aerosol particle mass analyzer (APM) in 1996 (Ehara et al. 1996) and the centrifugal particle mass analyzer (CPMA) in 2005 (Olfert 2005) has allowed for the additional classification of particles by mass (m) by the balance of centrifugal and electrostatic forces. The combination of D_m and m measured by a DMA in tandem with an APM or CPMA allow for the calculation of effective density (ρ_{eff}), mass-mobility exponent (D_{fm}) and effective dynamic shape factor (χ_{eff}) for particles < 1 μm (Ehara et al. 1996; McMurry et al. 2002; Olfert et al. 2007)

An extensive review by (Park et al. 2008) provides examples of tandem DMA measurements. Briefly explained here, variations in experimental design have used a DMA coupled with different aerosol measurement techniques. For example, a DMA and an electrical low-pressure impactor (ELPI) coupled system – set up in series set by (Maricq et al. 2000) and in parallel by (Virtanen et al. 2004) – determined D_m, D_{ae}, and ρ_{eff}. A DMA coupled with an optical particle counter and an aerodynamic particle sizer determined aerosol refractive index and ρ_{eff} (Hand and Kreidenweis 2002).

One drawback to the DMA, APM and CPMA is that these classification methods require the use of charged particles which presents complications in the analysis (Radney and Zangmeister 2016; Wang and Flagan 1990). To circumvent these issues, the aerodynamic aerosol classifier (AAC) was developed in 2013 (Tavakoli and Olfert 2013) and instead uses the response of the particle to an applied centrifugal force and counteracting drag force to determine the aerodynamic diameter (D_{ae}). The AAC was first demonstrated in a tandem AAC-DMA configuration by (Tavakoli and Olfert 2014) to measure the m, ρ_{eff}, D_{fm} and χ_{eff} of liquid dioctyl sebacate droplets and fresh soot. Utilizing this triad of instrumentation in combination allows for the determination of the dynamic shape factor (χ) and particle density (ρ_p).

Figure 1.

The pairwise collection of an AAC, DMA and APM (i.e. AAC-DMA, AAC-APM and DMA-APM) allows for independent determinations of D_{ae}, D_m and m and the derivation ρ_{eff} and χ, see Figure 1. Since the AAC, DMA and APM use different methods for aerosol classification (i.e. relaxation time, electrical mobility and mass-to-charge ratio), tandem combinations may

result in variations in measured properties. In this study, multiple combinations of tandem measurements (AAC-DMA, AAC-APM and DMA-APM) are utilized to determine m, ρ_{eff} and χ_{eff} for solid, nearly spherical particles composed of ammonium sulfate. The results from these three independent measurements are compared and discussed. Utilizing the triplet of instrumentation, we demonstrate the quantitative determination of χ and ρ_p for an aged black carbon mimic.

2. Materials and Methods

Block diagrams of the experimental setups to perform pairwise comparisons are shown in Figure 2. The sizing instruments were compared using ammonium sulfate (AS, 1 mg mL^{-1}) and a H_2O-dispersible black carbon aerosol mimic (CB, 0.2 mg mL^{-1}) that resembles aged, collapsed soot; see (Zangmeister et al. 2019) for a full description. Aerosols were generated from solution and suspension, respectively, using a constant output atomizer (TSI 3076)[1] and subsequently dried using a pair of silica gel diffusion dryers (TSI 3062). Size classification was performed by either an AAC (D_{ae}, Figure 2a, Cambustion) or a DMA (D_m, Figure 2b, TSI 3081 long DMA as part of a TSI 3080 electrostatic classifier).

Figure 2.

The D_{ae}-selected aerosol stream (Figure 2a) was charge neutralized using a soft x-ray source (TSI 3088) and sent to a parallel system consisting of a tandem DMA and condensation particle counter (CPC, TSI 3081 long DMA as part of a TSI 3082 electrostatic classifier with a TSI 3775 CPC) and a tandem APM (Kanomax 3602)-CPC (TSI 3775); raw data for AS can be found in Table S2 of the Supplementary Information. The flow through these systems was maintained at 300 cm^3 min^{-1} and 250 cm^3 min^{-1} by the CPCs. A cavity ring-down spectrometer is normally situated between the APM and CPC and receives a 50 cm^3 min^{-1} clean air backflush to prevent particle deposition on the mirrors (Radney and Zangmeister 2016). Although the CRD was in place, the CRD data was not utilized and will not be discussed in this analysis. D_{ae} selection spanned 150 nm to 550 nm (AS) or 150 nm to 400 nm (CB) with the aerodynamic size resolution (R_{ae}) of the AAC being maintained at 10 for all experiments. All reported data were generated from a single 5 min mobility diameter (D_m) or 10 min mass (m) distribution scan corresponding to 112 samples and ≈ 600 samples, respectively. Thus, the reported measurement results utilize Type B uncertainties (see Supplemental material) while reported averages utilize Type A uncertainties (1σ standard deviation across the data set).

The geometric mean mobility diameter, μ_{geo} (see Eq. 32), as a function of D_{ae} was determined from the AAC-DMA measurements. In the other experimental setup (Figure 2b), the aerosol stream was D_m-selected at this μ_{geo} and then passed to a parallel system consisting of a tandem DMA-CPC (i.e. scanning mobility particle sizer, SMPS) and a tandem APM-CPC; raw data for AS can be found in Table S3 of the Supplementary Information. DMA and APM measurements

[1] NIST Technical Disclaimer: Certain commercial equipment, instruments, or materials (or suppliers, or software, ...) are identified in this paper to foster understanding. Such identification does not imply recommendation or endorsement by the National Institute of Standards and Technology, nor does it imply that the materials or equipment identified are necessarily the best available for the purpose.

used sheath:aerosol flow of 10:1 and a classification parameter (λ_c) of 0.32, respectively (Ehara et al. 1996).

The operational parameters of the AAC and DMA were chosen to maintain an aerodynamic size resolution (R_{ae}, see Eq. 24) and mobility bandwidth ($\Delta Z_p/Z_p$, see Eq. 25) of 0.1, respectively. Unlike the DMA and AAC, the APM transfer function is an asymmetric trapezoid and the peak transmission efficiency is λ_c-dependent (Kuwata 2015). For the APM with $\lambda_c = 0.32$, $\Delta m/m$ in the negative and positive directions is to -0.24 and 0.27, respectively; see Figure 4. However, since m scales with D^3, the larger $\Delta m/m$ is comparable to the R_{ae} and $\Delta Z_p/Z_p$ of 0.1; see Section 3.4 for a complete discussion of the transfer functions.

The DMA used was calibrated using polystyrene latex spheres atomized from water prior to initiation of the described experiments. Additional details in the calibration and characterization of the DMA and APM are described in (Radney and Zangmeister 2016); results shown in Figure S1 of the Supplementary material. AAC performance was verified by the manufacturer at the beginning of this study and was re-evaluated by the manufacturer at the end of data collection.

3. Theory

The fundamental theory and operational parameters for the AAC, DMA and APM are well-known; see (Tavakoli and Olfert 2013), (Knutson and Whitby 1975) and (Ehara et al. 1996), respectively. Here we give an overview of the relevant theory to highlight the nuances between instruments that will be relevant to the presented results and discussion. As shown in Figure 3, particle classification by the AAC, DMA and APM rely on a combination of the non-contact forces: centrifugal (F_{cen}), drag (F_{drag}), and/or electrostatic (F_{elec}). In addition to these forces (black arrows), particle streamlines (grey dotted lines) and flows have been included; the centrifugal particle mass analyzer (CPMA) has also been included in Figure 3d for comparison to the APM. All figures are drawn with assuming the radial direction is upwards and flows progress from left to right.

Figure 3.

Both the aerodynamic diameter (D_{ae}) and the mobility diameter (D_m) quantified by the AAC and the DMA, respectively, are defined relative to a spherical particle. Spherical particles are often assumed, although not necessarily accurate. For comparing sizes, the volume equivalent diameter (D_{ve})

$$m = \rho_p \frac{\pi}{6} D_{ve}^3 \quad (1)$$

can be used where m is the particle mass and ρ_p is the particle density, including air voids. For homogeneous particles without air voids, $\rho_p = \rho_{bulk}$.

3.1. AAC.

Any particle moving at a constant velocity (v) experiences equal applied and drag forces

$$F_{\text{app}} = F_{\text{drag}} \quad (2)$$

where for a sphere in any flow regime (e.g. free-molecular, transition or continuum) (Kulkarni et al. 2011)

$$F_{\text{drag}} = \frac{v}{B_{\text{sp}}} \quad (3)$$

v and μ are the particle's velocity and the gas viscosity and B_{sp} is the mechanical mobility of a sphere

$$B_{\text{sp}} = \frac{C_{\text{c}}(D_{\text{sp}})}{3\pi\mu D_{\text{sp}}} \quad (4)$$

The drag force experienced by non-spherical particles is greater than that experienced by a volume equivalent sphere with the same velocity and flow regime effectively reducing B. The dynamic shape factor (χ) represents the ratio of B for a non-spherical particle (B_{non}) to that of the volume equivalent sphere (B_{ve}) (Kasper 1982)

$$\chi = \frac{B_{\text{ve}}}{B_{\text{non}}} = \frac{F_{\text{non}}\, v_{\text{ve}}}{F_{\text{ve}}\, v_{\text{non}}} \quad (5)$$

The Cunningham slip correction factor ($C_{\text{c}}(D)$) has been included to account for decreased drag in the free-molecular and transition regimes relative to the continuum regime. The generic form of the Cunningham slip correction factor $C_{\text{c}}(D)$ (Kulkarni et al. 2011) is

$$C_{\text{c}}(D) = 1 + \frac{2\lambda_{\text{g}}}{D}\left[1.142 + 0.558e^{\left(-0.999D/2\lambda_{\text{g}}\right)}\right] \quad (6)$$

where λ_{g} is the mean free path of the gas at the temperature (T) and pressure (P) of the measurement. For air at T = 298.15 K and P = 101.325 kPa: $\mu = 1.837 \times 10^{-5}$ kg m^{-1} s^{-1} and λ_{g} = 67.9 nm.

The rotating annular region of the AAC applies a centrifugal force (F_{cen})

$$F_{\text{cen}} = m\omega^2 r \quad (7)$$

where r and ω are the radial position of the particle and rotation speed, respectively. Thus,

$$\frac{v}{B_{\text{s}}} = m\omega^2 r \quad (8)$$

with the particle relaxation time (τ) defined as (Hinds 1999)

$$\tau \equiv mB_{\text{sp}} \quad (9)$$

Combining Eq. 8 and 9

$$\tau = \frac{v}{\omega^2 r} \quad (10)$$

allowing τ to be directly measured

$$\tau = \frac{Q_{\text{sh}} + Q_{\text{exh}}}{\pi\omega^2(r_1 + r_2)^2 L} \quad (11)$$

where Q_{sh}, Q_{exh}, r_1, r_2 and L are the sheath flow, exhaust flow, inner classifier radius (56 mm), outer classifier radius (60 mm) and the classifier length (206 mm), respectively. If operating under balanced flows, then $Q_{\text{sh}} = Q_{\text{exh}}$ and $Q_{\text{a}} = Q_{\text{s}}$ (the aerosol and sample flows, respectively) – see Figure 2a – and the numerator of Eq. 11 simplifies to $2Q_{\text{sh}}$.

The aerodynamic diameter (D_{ae}) is defined as the diameter of a sphere with standard density (ρ_0 = 1 g cm^{-3}) and the same velocity as that being measured. Since $m = \rho V$

$$\tau = \rho_p \frac{\pi}{6} D_{\text{sp}}^3 B_{\text{sp}} = \rho_0 \frac{\pi}{6} D_{\text{ae}}^3 \chi B_{\text{ae}} \quad (12)$$

which rearranges to

$$D_{\text{ae}} = D_{\text{sp}} \sqrt{\frac{\rho_{\text{p}} C_{\text{c}}(D_{\text{sp}})}{\chi \rho_0 C_{\text{c}}(D_{\text{ae}})}} \quad (13)$$

and it follows that

$$\tau = \frac{\rho_0 \chi D_{\text{ae}}^2 C_{\text{c}}(D_{\text{ae}})}{18\mu} \quad (14)$$

Note that determination of D_{ae} requires that either ρ_{p} and χ are known or assumed thus making D_{ae} an estimated parameter; χ = 1 is often assumed in Eq. 14 to allow this underdetermined system to be solved. An effective dynamic shape factor (χ_{eff}) is then determined from Eq. 13 as in (Kazemimanesh et al. 2019; Tavakoli and Olfert 2013; Tavakoli et al. 2014). In another instance, (Tavakoli and Olfert 2014) did not need to explicitly account for χ since only D_{ae} and D_{m}, not D_{ve}, were compared. See discussion below.

3.2. DMA.

In the DMA, an electric field is applied between two, usually concentric, electrodes – see Figure 2b – imparting and electrostatic force (F_{elec}) on the charged particles

$$F_{\text{elec}} = qeE \quad (15)$$

where q, e, and E are the net number of charges on the particle, the elementary electric charge ($\approx 1.602 \times 10^{-19}$ C) and the electric field strength, respectively. The electric mobility (Z_{p}) is (DeCarlo et al. 2004)

$$Z_{\text{p}} = qeB_{\text{m}} = \frac{qeC_{\text{c}}(D_{\text{m}})}{3\pi\mu D_{\text{m}}} \quad (16)$$

where D_{m} is defined as the diameter of a sphere with the same electrical mobility as that being measured. Combining Eq. 5 and 16,

$$\frac{D_{\text{m}}}{C_{\text{c}}(D_{\text{m}})} = \frac{\chi D_{\text{ve}}}{C_{\text{c}}(D_{\text{ve}})} \quad (17)$$

and D_{ve} does not necessarily equal D_{sp}. DMA measurements typically assume a single net charge is present on the particle. Z_p can be related to the physical dimensions of the classifier by

$$Z_p = \frac{Q_{sh}}{2\pi VL} \ln\left(r_2/r_1\right) \tag{18}$$

where r_1 = 0.937 cm, r_2 = 1.961 cm and L = 44.369 cm and V is the applied voltage.

3.3. APM.

The aerosol particle mass analyzer (APM) is essentially the combination DMA and AAC that is capable of directly measuring particle mass. The classifier rotates about an axis generating F_{cen} (Eq. 7) while an electric potential is applied to the inner electrode generating F_{elec} (Eq. 15); see Figure 2c. Thus,

$$F_{cen} = F_{elec} \tag{19}$$

and

$$m\omega^2 r = qeE = \frac{qeV}{r\ln\left(r_2/r_1\right)} \tag{20}$$

where r_1 = 24 mm and r_2 = 25 mm. As can be seen from Eq. 20, the APM classifies particles based upon their effective mass (m_{eff}) where

$$m_{eff} = \frac{m}{q} \tag{21}$$

During APM classification, the particles of interest will have no net radial velocity and F_{drag} = 0. The result is that the APM directly measures particle mass without any assumptions of particle shape (χ) but does assume a single net charge. If ρ_p is known, then D_{ve} can be directly calculated from Eq. 1, otherwise, in combination with a DMA, the effective density ρ_{eff} is calculated as

$$\rho_{eff} = \frac{m}{(\frac{\pi}{6})D_m^3} \tag{22}$$

It is worth mentioning that the Cambustion centrifugal particle mass analyzer (CPMA) – see Figure 2d – operates similarly to the Kanomax APM except that the inner electrode rotates slightly faster than the outer electrode causing F_{cen} to decrease with radius. This causes particles to exhibit a stable flow for a larger fraction of the operating area impacting the transfer function. We direct the reader to (Olfert and Collings 2005) and (Sipkens et al. 2020b) for an in-depth comparison of the APM and CPMA.

3.4. Transfer functions.

Thus far, the transfer functions of the AAC, DMA and APM have been treated as Dirac delta functions. The actual transfer functions have finite widths that are a function of the operating parameters. Since the AAC, DMA and APM utilize different mechanisms for particle

classification (relaxation time, electrical mobility and mass-to-charge ratio) these resolutions are often reported utilizing different metrics: relaxation time (R_τ) or aerodynamic size (R_{ae}) resolution, sheath:aerosol flow and the classification parameter (λ_c), respectively. Here, we relate these resolution metrics to the height and full width of the transfer functions at baseline.

For the AAC, the relaxation time resolution (R_τ) is defined based upon the ratio of Q_{sh} to Q_{aero} and assumes that these flows are balanced, laminar and constant:

$$\frac{1}{R_\tau} = \frac{\Delta\tau}{\tau} = \frac{Q_{aero}}{Q_{sh}} \tag{23}$$

The AAC transfer function is an isosceles triangle with respect to relaxation time. The fraction of particles transmitted at τ, $t(\tau) = 1.0$, and drops to 0 at $\tau \pm R_\tau$ (Tavakoli and Olfert 2013). Rather than utilizing R_τ, the AAC resolution can be defined based upon the aerodynamic diameter resolution (R_{ae})

$$\frac{1}{R_{ae}} = \frac{\Delta D_{ae}}{D_{ae}} \tag{24}$$

For constant R_{ae}, the rotation speed and sheath flow of the AAC are a function of the classified particles. Presently, $R_{ae} = 10$ with Q_{sh} and ω adjusted accordingly by the instrument. The full width of the transfer function is two times R_{ae} and is 0.2 ($R_{ae} = 10$).

For the DMA – assuming laminar flow and that the particles are non-diffusing – the transfer function is an isosceles triangle with respect to the electrical mobility (Z_p). The fraction of particles transmitted at Z_p, $t(Z_p) = 1.0$ (Hagwood et al. 1999; Knutson and Whitby 1975; Kuwata 2015) and drops to 0 at $Z_p \pm \Delta Z_p$ where

$$\frac{\Delta Z_p}{Z_p} = \frac{Q_{aero}}{Q_{sh}} \tag{25}$$

The full width of the transfer function is two times $\Delta Z_p/Z_p$ and for the present measurements is 0.2 ($Q_{sh}/Q_{aero} = 10$). The Z_p dependence of the DMA transfer function causes it to be asymmetric with respect to D_m.

The transfer function of the APM – assuming uniform laminar flow – is an asymmetric trapezoid with a center at m_{eff} (Kuwata 2015; Lall et al. 2009; Lall et al. 2008). The APM classification parameter (λ_c) is

$$\lambda_c = \frac{2\tau\omega^2 L}{v} \tag{26}$$

and represents the ratio of the axial (L/v) and radial ($1/2\tau\omega^2$) transversal times of an uncharged particle. Following (Kuwata 2015), the width of the transfer function at baseline in the positive and negative directions ($\Delta m^+/m_s$ and $\Delta m^-/m_s$, respectively, or $\Delta m^\pm/m_s$ collectively) is

$$\frac{\Delta m^\pm}{m_{eff}} = -2\ln\left[1 \mp \left(\frac{\delta}{r_c}\right)\coth\left(\frac{\lambda_c}{2}\right)\right] \tag{27}$$

where

$$\delta = \frac{(r_1 - r_2)}{2} \tag{28}$$

and the center of the classification region (r_c)

$$r_c = \frac{(r_1 + r_2)}{2} \tag{29}$$

r_1 and r_2 are the radius of the inner (24 mm) and outer (25 mm) electrodes, respectively. The transmission probability is

$$t(m) = e^{-\lambda_c} \tag{30}$$

spanning from

$$\frac{\Delta m_2^{\pm}}{m_{eff}} = -2\ln\left(1 \mp \frac{\delta}{r_c}\right) \tag{31}$$

Presently, $\lambda_c = 0.32$ corresponding to $\Delta m^-/m_{eff} = 0.242$ and $\Delta m^+/m_{eff} = 0.275$ and $t(m_{eff}) = 0.73$.

The DMA, AAC and APM transfer functions in their native measurands (Z_p, D_{ae} and m) are plotted in Figures 4a through 4c, respectively. The combined values transformed to D_{ve} are shown in Figure 4d utilizing the operational parameters outlined above. The absolute widths of the transfer functions will scale with size, so these values should be considered representative for this D_{ve}. For these calculations, a spherical AS particle with a physical diameter of 250 nm and bulk density was assumed; *i.e.* $D_p = D_m = D_{ve} = 250$ nm, $\rho_p = \rho_{eff} = \rho_{bulk} = 1.77$ g cm^{-3}, $\chi = 1$, $m_p = 14.4$ fg and $D_{ae} = 356$ nm.

Figure 4.

Note, the transfer function calculated in Figure 4c is for the APM and not the CPMA. The CPMA transfer function has a similar trapezoidal shape but higher $t(m) = 1$ independent of λ_c; see (Olfert and Collings 2005) and (Sipkens et al. 2020b) for detailed comparisons of the APM and CPMA transfer functions.

3.5. Data inversions.

Scanning measurements by the AAC, DMA or APM are often performed and the data must be inverted in order to determine the underlying particle distributions; e.g. (Mai and Flagan 2018) and (Stolzenburg 2018) for the DMA and (Rawat et al. 2016) and (Sipkens et al. 2020a) for the DMA-APM. However, in the present work, data inversions were not performed since the parameters of interest (D_{ae}, D_m and m for the AAC, DMA and APM, respectively) could be determined directly from the instrumental setpoint (D_{ae} and D_m) or from fitting the distributions of the scanned data (D_m and m). We assume that the aerosol concentration is constant over the width of the transfer functions (Stolzenburg and McMurry 2018) but expect this assumption to have little impact on our measurements since: 1) the geometric or arithmetic means are the quantity of interest and 2) these deviations are small relative to the instrumentally imposed measurement resolution.

3.6. Multiple charging.

All classification methods that are charge dependent suffer from multiple charging issues ($|q| > 1$) and this is especially true for the DMA and APM. Prior to classification by these instruments, the aerosol stream is passed through a charge neutralizer (*N in Figure 2) to impart a known bipolar charge distribution to the particles (Tigges et al. 2015; Wiedensohler and Fissan 1988). The q of particles exiting the charge neutralizer is a strong function of particle size, shape (Rogak et al. 1993), neutralizer age and type (Tigges et al. 2015), and to a lesser extent particle morphology (Covert et al. 1997).

To demonstrate these multiple charging artifacts, we performed tandem DMA (TDMA) measurements whereby particles exiting an upstream DMA are passed through a second neutralizer and DMA and the corresponding size distribution was measured; see Figure 2b. A representative TDMA size distribution is shown in Figure 5a for AS aerosol with a nominal $D_{ae} \approx 250$ nm ($D_m = 169$ nm). The notation $q \rightarrow q$' in Figure 4a denotes the charge of particles exiting the first and second DMAs, respectively. The size distribution exhibits multiple peaks beyond just that selected by the upstream DMA ($D_m = 169$ nm); in the case of $D_m = 169$ nm (green line), the peak is composed primarily of particles with $q = q' = +1$ with smaller fractions of $q = q' = +2$ and +3 also present (Mamakos 2016). In addition, $q \rightarrow q'$ of +2 → +1, +3 → +1, +1 → +2, +1 → +3, +2 → +3 and +3 → +2 are observed at $D_m = 265.2$ nm, 352.9 nm, 110.1 nm, 87.33 nm, ≈ 217 nm and ≈ 131 nm, respectively. To determine D_m, the mobility distributions were fit utilizing multiple log-normal distributions

$$N = \sum_{i=1}^{n} A_i * exp\left(\frac{-1 * (\log D_m - \mu_{geo,i})^2}{2\sigma_{geo,i}^2}\right) \quad (32)$$

and A, μ_{geo} and σ_{geo} are the peak amplitude, the geometric mean diameter and the geometric standard deviation. For consistency, we will continue to refer to fitted μ_{geo} as the D_m of as distribution. The summation and the i subscripts denote that all peaks with $N > 7.5 \times 10^8$ m^{-3} were included in the fit. Other higher order multiples could also be present but unresolved – e.g. +4 → +2, +6 → +3, etc. (Mamakos 2016) – since the soft x-ray neutralizer produces a greater fraction of $q > +1$ than the radioactive neutralizers (Tigges et al. 2015). These redistributed charges are only present in the TDMA measurements and only apply to the illustrative data presented here. Even if a significant number of higher order charges are present, they are not expected to impact the determination of D_m.

Figure 5.

To determine the average particle mass, the distribution of N as a function of m was measured by the APM and were fit utilizing multiple Gaussian distributions

$$N = \sum_{q=1}^{n} A_q * \exp\left(\frac{-(m - m_{eff,q})^2}{2\sigma_{eff,q}^2}\right) \quad (33)$$

where A, m and σ correspond to the peak amplitude, the mass and the width (i.e. standard deviation) of the distribution. Similar to D_m (Eq. 32), and for consistency throughout, we will continue to refer to the average mass of the distribution ($m_{eff,q}$) as m. The summations and q have been included to denote that all peaks with $q \geq +1$ were included in the fit; see Figure 5b. In

instances where particles are non-spherical with low effective densities, even this approach has its limitations (Radney et al. 2014).

When performing DMA-APM measurements, the particles are not sent through a 2nd charge neutralizer prior to the APM. Thus, all particles exiting the DMA having a common electrical mobility with physical diameters (and hence masses) that scale with charge as shown by the +2 → +1 (cyan) and +3 → +1 (blue) traces in Figure 5a. These particles bearing larger charges can also be seen in the mass distributions of N as shown in Figure 5b.

Separation of particles by an AAC, versus a DMA, poses slightly different challenges when combined with a downstream DMA or APM (Figure 2a). The AAC separates particles based upon their relaxation time to an applied centrifugal force and is charge independent. However, upon passing from the AAC to either a DMA or APM, the particles must pass through a charge neutralizer in order to reach an equilibrium bipolar charge distribution independent of the incoming charge state (Wiedensohler and Fissan 1988). This causes the size distribution to exhibit multiple peaks where all particles have a common D_{ae} but a q-dependent D_m; see Figure 6a for AAC-DMA measurements of AS with D_{ae} = 350 nm. In the AAC-APM, versus the DMA-APM, the contributions of particles bearing $q > +1$ cannot necessarily be isolated as seen in Figure 6b.

Figure 6.

For the purpose of comparing the tandem measurements (AAC-DMA, AAC-APM and DMA-APM) the quantities of interest will derive from the geometric and arithmetic means of the measured size and mass distributions by the DMA and APM, respectively. As a result, the impact of multiple charging on the reported results is only expected to be significant for smaller particles where overlap between successive charges increases. Non-spherical particles with low effective densities, such as fresh soot, would exhibit similar problems but are not considered here; e.g. (Radney et al. 2014) and (Tavakoli and Olfert 2014). The smallest AS particles measured presently had $D_m \approx 100$ nm with $\rho_p = 1.77$ g cm^{-3} while for CB the smallest $D_m \approx$ 150 nm and $\rho_p = 1.00$ g cm^{-3} so the multiple charging effects are resolvable.

3.7. Comparing tandem measurements.

A fundamental objective of this manuscript is to compare the measured and derived parameters from each of the tandem techniques (AAC-DMA, AAC-APM and DMA-APM); see Figures 1 and 2. In the case of the AAC-DMA, τ and Z_p are measured (Eq. 11 and 18, respectively) from which B (Eq. 16), and hence m (Eq. 9) can be calculated. For the AAC-APM, τ and m are measured (Eq. 11 and 20, respectively), from which B (Eq. 9), and hence D_m (Eq. 16) can be calculated. For the DMA-APM, Z_p and m are measured (Eq. 17 and 20, respectively) from which B, and hence τ (Eq. 9) can be determined. D_{ae} is determined from τ in all configurations assuming $\chi = 1$ (Eq. 14). For all tandem combinations, a ρ_p must be assumed in order to estimate D_{ve} (Eq. 1) and χ_{eff} (Eq. 5).

4. Results and Discussion

4.1. Ammonium sulfate

In principle, measured pairwise combinations of τ (D_{ae}), Z_p (D_m) and/or m by an AAC, DMA and/or APM, respectively, can be used to derive the third quantity (as shown in Figure 1). In one configuration, particles were classified by D_{ae} with the AAC and D_m and m_p were measured in parallel (Figure 2a). For direct comparability between measurements, in the second configuration (Figure 2b), particles were classified by the DMA using the measured D_m from the AAC-DMA. As a result, the D_m data from the DMA-APM has not been included in the D_m comparisons (see Figure 7a and 9a).

In the case of AS, the calculated D_m (AAC-APM, red squares) were consistently smaller than the measured D_m (AAC-DMA, black circles), see Figure 7a, with an average deviation of (-4 ± 1) % (Figure 7b). The relative deviations between measurements (i) are calculated as

$$\frac{(i_a - i_b)}{i_b} \times 100\% \quad (34)$$

The relative deviations of Figures 7b and 9b were calculated with a representing the AAC-APM and b the AAC-DMA. For all other calculations of relative deviation (Figures 7d, 7f, 7h, 9b, 9f and 9h), a represents either the AAC-DMA or AAC-APM and b the DMA-APM.

The AAC-DMA measures τ and Z_p from which the D_{ae} (Eq. 14) and D_m (Eq. 16) are derived. Similar to the investigations of (Kazemimanesh et al. 2019; Tavakoli and Olfert 2013; Tavakoli et al. 2014), we assume that $\chi = 1$ in Eq. 14 allowing for D_{ae} to be calculated; χ_{eff} is later calculated from D_{ve}. The m calculated from the AAC-DMA can be compared to the m directly measured by the AAC-APM and DMA-APM; see Figure 7c. In general, the AAC-DMA tends to report the highest m of all measurements. The average m deviation between the DMA-APM and the AAC-DMA and the AAC-APM are (9 ± 5) % and (4 ± 5) % for AS, respectively. All measures of m agree within 15%.

Figure 7.

Particle effective density (ρ_{eff}) is an important parameter that can serve as a metric of particle morphology and may be used to convert size distributions to mass distributions or from mobility distributions to aerodynamic distributions (Johnson et al. 2018); the μ_{geo} of the D_m fits were utilized in the calculation of ρ_{eff}, see Eq. 22 and 32.The average ρ_{eff} for AS spanning 150 nm ≤ D_{ae} ≤ 550 nm are (1.62 ± 0.02) g cm^{-3}, (1.75 ± 0.01) g cm^{-3} and (1.91 ± 0.04) g cm^{-3} for the DMA-APM, AAC-DMA and AAC-APM, respectively. The % deviations are (8 ± 2) % and (18 ± 3) % for the AAC-DMA and AAC-APM versus the DMA-APM, respectively (Figure 7f). Notably, the ρ_{eff} determined from the AAC-APM measurements are not physically reasonable considering the bulk density of AS is 1.77 g cm^{-3} and these particles are not expected to be perfectly spherical and may contain voids (Zelenyuk et al. 2006).

The dynamic shape factor (χ) is another useful metric for quantifying particle morphology. It is defined as the ratio of the drag force experienced by a non-spherical particle to the drag force

experienced by a volume-equivalent spherical particle with the same velocity and flow regime with values of 1 for perfect spheres and >> 1 for lacey aggregates. In the case of AS, the DMA-APM, AAC-DMA and AAC-APM yielded χ_{eff} of 1.05 ± 0.01, 1.006 ± 0.005, 0.97 ± 0.03, respectively; we refer to these as effective dynamic shape factors (χ_{eff}) because a particle density (ρ_p) – here $\rho_p = \rho_{bulk}$ = 1.77 g cm^{-3} – must be assumed. This is different than the dynamic shape factor (χ) determined for CB below from the triplet of instruments where ρ_p is not assumed. The deviations are (-4 ± 1) % and (-8 ± 1) % for the AAC-DMA and AAC-APM versus the DMA-APM, respectively. As with ρ_{eff}, the AAC-APM measurements are not physically reasonable (χ < 1), even though all measurements are within 8 % of each other.

4.2. Data harmonization

The governing behavior of the classifiers (AAC, DMA and APM) and associated mathematical relationships are highly interconnected due to their similarity (see Figure 3). On average there is an 8 % deviation in ρ_{eff} between the AAC-DMA, (1.75 ± 0.01) g cm^{-3}, and the DMA-APM, (1.62 ± 0.02) g cm^{-3} and an 18 % deviation between the DMA-APM and the AAC-APM, (1.91 ± 0.04) g cm^{-3}. If instead ρ_{eff} was calculated with the D_m from the AAC-DMA and m_p from the AAC-APM, ρ_{eff} = (1.66 ± 0.1) g cm^{-3} and the deviation decreases to 2.7 %; within measurement uncertainty (see Table S1 of Supplemental Material for uncertainties). This indicates that the m calculated from the AAC-DMA and D_m calculated from the AAC-APM are responsible for the deviations.

The relaxation time ($\tau = mB$, Eq. 9) assumes sphericity. However, the mass that of interest is for a non-spherical particle (AS) requiring that χ be included in Eq. 9; i.e.

$$m = \frac{\tau}{\chi B_m} \tag{35}$$

Utilizing χ_{eff} from the DMA-APM to calculate m in Eq. 35 decreases the average ρ_{eff} from (1.75 ± 0.01) g cm^{-3} to (1.67 ± 0.02) g cm^{-3} with a deviation of 3.4 %, nearly within the calculated uncertainty of 2.9 % and 3.2 % for the AAC-DMA and DMA-APM, respectively. This also implies that the D_{ae} calculated from τ should also be decreased by ≈ $\sqrt{\tau}$ (Eq. 14).

Like τ, D_m assumes sphericity, so the actual particle mobility will be smaller by a factor of χ. Utilizing χ_{eff} from the DMA-APM to calculate D_m for the AAC-APM decreases ρ_{eff} from (1.91 ± 0.04) g cm^{-3} to (1.62 ± 0.02) g cm^{-3} and the deviation is < 1 %.

The observations presented above demonstrate that data harmonization between the DMA-APM, AAC-DMA and AAC-APM requires the use of χ since it is the conversion factor between sphericity and non-sphericity. To a lesser extent, data harmonization could also be impacted by: 1) the assumed physical and thermodynamic parameters (μ = 18.3245 × 10^{-6} Pa s and λ_g= 68.29 nm at T = 295.61 K and P = 99.6 kPa) and 2) the Cunningham slip correction factor which is dependent upon both the surface roughness and the physical state (solid or liquid) of the particle (Allen and Raabe 1985) and have uncertainties on the order of 1.2 % (Tavakoli and Olfert 2014) and 2.1 % (Allen and Raabe 1985), respectively.

(Tavakoli and Olfert 2014) measured the ρ_{eff} of dioctyl sebacate (DOS), an organic liquid, using the AAC-DMA and obtained ρ_{eff} that agreed very well with ρ_{bulk}: (0.903 ± 0.090) g cm^{-3} versus (0.913 ± 0.003) g cm^{-3}, respectively, a -1.1 % difference. We attribute this agreement to the fact that DOS is a liquid and forms smooth, spherical, void-free particles (i.e. $\chi = 1$ so $C_c(D)$ is well-known) and so the analysis above was not necessary. However, it is possible that the soot masses of (Tavakoli and Olfert 2014) could be in error since χ was not utilized in the determination of m, but rather calculated afterwards. For CB (see below), this distinction results in the calculated mass being ≈ 10 % higher than measured.

4.3. Carbon black

In addition to AS, an aged black carbon mimic (CB) was also investigated. Unlike AS, which is a solid and nearly-spherical, the CB particles consists of spherical monomers ≈ 30 nm in diameter agglomerated into a larger particle with a compacted morphology (You et al. 2016). Utilizing the combination of τ, B (from D_m) and m measured by the AAC, DMA and APM – tandem configuration of Figure 2a – χ (Eq. 35) and ρ_p (Eq. 1) were be quantitatively determined to be 1.09 ± 0.03 and (1.00 ± 0.03) g cm^{-3}, respectively, with a minor size dependence; see Table 1. Assuming ρ_{bulk} = 1.8 g cm^{-3} for CB, this implies that CB has a packing density (θ_f) of 0.55 ± 0.02 which higher than expected for soot compacted through water condensation and evaporation (Zangmeister et al. 2014).

Table 1.

5. Summary

The AAC, DMA and APM measure the aerodynamic diameter (D_{ae} from τ), mobility diameter (D_m from Z_p) and mass (m). Combining these three measurements allow for the dynamic shape factor (χ) and particle density (ρ_p) to be determined quantitatively. However, the use of two out of the three quantities to define mass, size, shape and/or density is subject to uncertainty. Specifically, mass and size values determined by these three configurations vary by up to 10 % causing the effective density to vary by up to 18 %. More importantly, non-physical values are sometimes reported. Further errors can arise, especially when utilizing an AAC, from assuming a dynamic shape factor (χ). Physical conditions are also important but to a lesser extent than χ; e.g. T and P affect the gas viscosity, mean free path and Cunningham slip correction factor therefore impacting D_m and D_{ae}. Uncertainties in the effective dynamic shape factor can easily be greater than 10 % when utilizing a paired combination of instruments with the triplet circumventing these issues. Understanding these differences is required to harmonize methods, improve data agreement and enable quantitative comparability between studies.

Acknowledgements

This study was supported by the Greenhouse Gas Measurements Program at the National Institute of Standards and Technology and the U.S. National Science Foundation (NSF) under Grant 1708337. Its contents are solely the responsibility of the grantee and does not necessarily

represent the official views of the NSF. Furthermore, the NSF does not endorse the purchase of any commercial products or services mentioned in the publication.

Definitions

AAC	Aerodynamic aerosol classifier
APM	Aerosol particle mass analyzer
AS	Ammonium sulfate
B	Mechanical mobility (m N^{-1} s^{-1})
C_c	Cunningham slip correction factor
χ	Dynamic shape factor
CB	Carbon black
CPMA	Centrifugal particle mass analyzer
CPC	Condensation particle counter
D	Diameter (nm)
DMA	Differential mobility analyzer
Δx	Width of x's transfer function
e	Elementary charge ($\approx 1.602 \times 10^{-19}$ C)
F	Force (N)
L	Length (cm)
λ_c	APM classification parameter
λ_g	Mean free path (nm)
m	Mass (fg)
μ	Gas viscosity (kg m^{-1} s^{-1})
μ_{geo}	Geometric mean diameter (nm)
N	Number density of particles (m^{-3})
P	Pressure (kPa)
q	Net charge
Q	Flow
r	Radius (cm)
R	Resolution
ρ	Density
σ	Distribution width
T	Temperature (K)
τ	Relaxation time (ns)
V	Voltage (V)
Z_p	Electrical mobility (m^2 V^{-1} s^{-1})
ω	Rotation speed (rotations min^{-1})

Subscripts

ae	aerodynamic
aero	aerosol
bulk	bulk
c	center
eff	effective
m	mobility
non	non-spherical

p	particle
s	sample
sh	sheath
sp	spherical
ve	volume equivalent
1	inner
2	outer

References

Allen, M. D. and Raabe, O. G. (1985). Slip Correction Measurements of Spherical Solid Aerosol Particles in an Improved Millikan Apparatus. *Aerosol Science and Technology* 4:269-286. DOI: 10.1080/02786828508959055

Covert, D., Wiedensohler, A., Russell, L. (1997). Particle Charging and Transmission Efficiencies of Aerosol Charge Neutralizes. *Aerosol Science and Technology* 27:206-214. DOI: 10.1080/02786829708965467

DeCarlo, P. F., Slowik, J. G., Worsnop, D. R., Davidovits, P., Jimenez, J. L. (2004). Particle Morphology and Density Characterization by Combined Mobility and Aerodynamic Diameter Measurements. Part 1: Theory. *Aerosol Science and Technology* 38:1185-1205. DOI: 10.1080/027868290903907

Ehara, K., Hagwood, C., Coakley, K. J. (1996). Novel method to classify aerosol particles according to their mass-to-charge ratio—Aerosol particle mass analyser. *Journal of Aerosol Science* 27:217-234. DOI: 10.1016/0021-8502(95)00562-5

Hagwood, C., Sivathanu, Y., Mulholland, G. (1999). The DMA Transfer Function with Brownian Motion a Trajectory/Monte-Carlo Approach. *Aerosol Science and Technology* 30:40-61. DOI: 10.1080/027868299304877

Hand, J. L. and Kreidenweis, S. M. (2002). A New Method for Retrieving Particle Refractive Index and Effective Density from Aerosol Size Distribution Data. *Aerosol Science and Technology* 36:1012-1026. DOI: 10.1080/02786820290092276

Hinds, W. C. (1999). Aerosol Technology: Properties, Behavior, and Measurement of Airborne Particles. John Wiley & Sons, Inc., New York, NY.

Johnson, T. J., Irwin, M., Symonds, J. P. R., Olfert, J. S., Boies, A. M. (2018). Measuring aerosol size distributions with the aerodynamic aerosol classifier. *Aerosol Science and Technology* 52:655-665. DOI: 10.1080/02786826.2018.1440063

Kasper, G. (1982). Dynamics and Measurement of Smokes. I Size Characterization of Nonspherical Particles. *Aerosol Science and Technology* 1:187-199. DOI: 10.1080/02786828208958587

Kazemimanesh, M., Moallemi, A., Thomson, K., Smallwood, G., Lobo, P., Olfert, J. S. (2019). A novel miniature inverted-flame burner for the generation of soot nanoparticles. *Aerosol Science and Technology* 53:184-195. DOI: 10.1080/02786826.2018.1556774

Knutson, E. O. and Whitby, K. T. (1975). Aerosol classification by electric mobility: apparatus, theory, and applications. *Journal of Aerosol Science* 6:443-451. DOI: 10.1016/0021-8502(75)90060-9

Kulkarni, P., Baron, P. A., Willeke, K., eds. (2011). Aerosol Measurement: Principles, Techniques and Applications. John Wiley & Sons, Inc., Hoboken, NJ. DOI: 10.1002/9781118001684

Kuwata, M. (2015). Particle Classification by the Tandem Differential Mobility Analyzer–Particle Mass Analyzer System. *Aerosol Science and Technology* 49:508-520. DOI: 10.1080/02786826.2015.1045058

Lall, A. A., Ma, X., Guha, S., Mulholland, G. W., Zachariah, M. R. (2009). Online Nanoparticle Mass Measurement by Combined Aerosol Particle Mass Analyzer and Differential Mobility Analyzer: Comparison of Theory and Measurements. *Aerosol Science and Technology* 43:1075-1083. DOI: 10.1080/02786820903095484

Lall, A. A., Rong, W., Mädler, L., Friedlander, S. K. (2008). Nanoparticle aggregate volume determination by electrical mobility analysis: Test of idealized aggregate theory using aerosol particle mass analyzer measurements. *Journal of Aerosol Science* 39:403-417. DOI: 10.1016/j.jaerosci.2007.12.010

Mai, H. and Flagan, R. C. (2018). Scanning DMA Data Analysis I. Classification Transfer Function. *Aerosol Science and Technology* 52:1382-1399. DOI: 10.1080/02786826.2018.1528005

Mamakos, A. (2016). Methodology to quantify the ratio of multiple-to single-charged fractions acquired in aerosol neutralizers. *Aerosol Science and Technology* 50:363-372. DOI: 10.1080/02786826.2016.1153034

Maricq, M. M., Podsiadlik, D. H., Chase, R. E. (2000). Size Distributions of Motor Vehicle Exhaust PM: A Comparison Between ELPI and SMPS Measurements. *Aerosol Science and Technology* 33:239-260. DOI: 10.1080/027868200416231

McMurry, P. H., Wang, X., Park, K., Ehara, K. (2002). The Relationship between Mass and Mobility for Atmospheric Particles: A New Technique for Measuring Particle Density. *Aerosol Science and Technology* 36:227-238. DOI: 10.1080/027868202753504083

Olfert, J. S. (2005). A Numerical Calculation of the Transfer Function of the Fluted Centrifugal Particle Mass Analyzer. *Aerosol Science and Technology* 39:1002-1009. DOI: 10.1080/02786820500380222

Olfert, J. S. and Collings, N. (2005). New method for particle mass classification—the Couette centrifugal particle mass analyzer. *Journal of Aerosol Science* 36:1338-1352. DOI: 10.1016/j.jaerosci.2005.03.006

Olfert, J. S., Symonds, J. P. R., Collings, N. (2007). The effective density and fractal dimension of particles emitted from a light-duty diesel vehicle with a diesel oxidation catalyst. *Journal of Aerosol Science* 38:69-82. DOI: 10.1016/j.jaerosci.2006.10.002

Park, K., Dutcher, D., Emery, M., Pagels, J., Sakurai, H., Scheckman, J., Qian, S., Stolzenburg, M. R., Wang, X., Yang, J., et al. (2008). Tandem Measurements of Aerosol Properties—A Review of Mobility Techniques with Extensions. *Aerosol Science and Technology* 42:801-816. DOI: 10.1080/02786820802339561

Radney, J. G., You, R., Ma, X., Conny, J. M., Zachariah, M. R., Hodges, J. T., Zangmeister, C. D. (2014). Dependence of Soot Optical Properties on Particle Morphology: Measurements and Model Comparisons *Environmental Science & Technology* 48:3169-3176. DOI: 10.1021/es4041804

Radney, J. G. and Zangmeister, C. D. (2016). Practical limitations of aerosol separation by a tandem differential mobility analyzer–aerosol particle mass analyzer. *Aerosol Science and Technology* 50:160-172. DOI: 10.1080/02786826.2015.1136733

Rawat, V. K., Buckley, D. T., Kimoto, S., Lee, M.-H., Fukushima, N., Hogan Jr, C. J. (2016). Two dimensional size–mass distribution function inversion from differential mobility analyzer–aerosol particle mass analyzer (DMA–APM) measurements. *Journal of Aerosol Science* 92:70-82. DOI: 10.1016/j.jaerosci.2015.11.001

Rogak, S. N., Flagan, R. C., Nguyen, H. V. (1993). The Mobility and Structure of Aerosol Agglomerates. *Aerosol Science and Technology* 18:25-47. DOI: 10.1080/02786829308959582

Sipkens, T. A., Olfert, J. S., Rogak, S. N. (2020a). Inversion methods to determine two-dimensional aerosol mass-mobility distributions: A critical comparison of established methods. *Journal of Aerosol Science* 140:105484. DOI: 10.1016/j.jaerosci.2019.105484

Sipkens, T. A., Olfert, J. S., Rogak, S. N. (2020b). New approaches to calculate the transfer function of particle mass analyzers. *Aerosol Science and Technology* 54:111-127. DOI: 10.1080/02786826.2019.1680794

Stolzenburg, M. R. (2018). A Review of Transfer Theory and Characterization of Measured Performance for Differential Mobility Analyzers. *Aerosol Science and Technology*:1-75. DOI: 10.1080/02786826.2018.1514101

Stolzenburg, M. R. and McMurry, P. H. (2018). Accuracy of recovered moments for narrow mobility distributions obtained with commonly used inversion algorithms for mobility size spectrometers. *Aerosol Science and Technology* 52:614-625. DOI: 10.1080/02786826.2018.1455963

Tavakoli, F. and Olfert, J. S. (2013). An Instrument for the Classification of Aerosols by Particle Relaxation Time: Theoretical Models of the Aerodynamic Aerosol Classifier. *Aerosol Science and Technology* 47:916-926. DOI: 10.1080/02786826.2013.802761

Tavakoli, F. and Olfert, J. S. (2014). Determination of particle mass, effective density, mass–mobility exponent, and dynamic shape factor using an aerodynamic aerosol classifier and a differential mobility analyzer in tandem. *Journal of Aerosol Science* 75:35-42. DOI: 10.1016/j.jaerosci.2014.04.010

Tavakoli, F., Symonds, J. P. R., Olfert, J. S. (2014). Generation of a Monodisperse Size-Classified Aerosol Independent of Particle Charge. *Aerosol Science and Technology* 48:i-iv. DOI: 10.1080/02786826.2013.877121

Tigges, L., Wiedensohler, A., Weinhold, K., Gandhi, J., Schmid, H. J. (2015). Bipolar charge distribution of a soft X-ray diffusion charger. *Journal of Aerosol Science* 90:77-86. DOI: 10.1016/j.jaerosci.2015.07.002

Virtanen, A., Ristimäki, J., Keskinen, J. (2004). Method for Measuring Effective Density and Fractal Dimension of Aerosol Agglomerates. *Aerosol Science and Technology* 38:437-446. DOI: 10.1080/02786820490445155

Wang, S. C. and Flagan, R. C. (1990). Scanning Electrical Mobility Spectrometer. *Aerosol Science and Technology* 13:230-240. DOI: 10.1080/02786829008959441

Wiedensohler, A. and Fissan, H. J. (1988). Aerosol charging in high purity gases. *Journal of Aerosol Science* 19:867-870. DOI: 10.1016/0021-8502(88)90054-7

You, R., Radney, J. G., Zachariah, M. R., Zangmeister, C. D. (2016). Measured Wavelength-Dependent Absorption Enhancement of Internally Mixed Black Carbon with Absorbing and Nonabsorbing Materials. *Environmental Science & Technology* 50:7982-7990. DOI: 10.1021/acs.est.6b01473

Zangmeister, C. D., Grimes, C. D., Dickerson, R. R., Radney, J. G. (2019). Characterization and demonstration of a black carbon aerosol mimic for instrument evaluation. *Aerosol Science and Technology*:1-12. DOI: 10.1080/02786826.2019.1660302

Zangmeister, C. D., Radney, J. G., Dockery, L. T., Young, J. T., Ma, X., You, R., Zachariah, M. R. (2014). Packing density of rigid aggregates is independent of scale. *Proceedings of the National Academy of Sciences of the United States of America* 111:9037-9041. DOI: 10.1073/pnas.1403768111

Zelenyuk, A., Cai, Y., Imre, D. (2006). From agglomerates of spheres to irregularly shaped particles: Determination of dynamic shape factors from measurements of mobility and vacuum aerodynamic diameters. *Aerosol Science and Technology* 40:197-217. DOI: 10.1080/02786820500529406

Figure 1. Schematic representation of the instruments and the corresponding measured values – mobility diameter (D_m), aerodynamic diameter (D_{ae}) and particle mass (m) – the tandem measurement pairs (connected by lines) and the corresponding derived values. Pairwise combination allows for determination of effective density (ρ_{eff}) and effective dynamic shape factor (χ_{eff}). The combination of all three measurements allows for the quantitative determination of the dynamic shape factor (χ) and particle density (ρ_p). The circle (black), square (red) and triangle (green) are used throughout the manuscript to denote the corresponding measurement results.

Figure 2. Block diagram of the two experimental setups (a and b) used in this study to achieve three configurations (AAC-DMA, AAC-APM, DMA-APM). *N corresponds to soft x-ray charge neutralizer.

Figure 3. Forces (F), flows (Q), axes of rotation (ω) and particle trajectories (dotted grey lines) in the a) aerodynamic aerosol classifier (AAC), b) differential mobility analyzer (DMA), c) the aerosol particle mass analyzer (APM) and d) the centrifugal particle mass analyzer (CPMA). All figures are oriented with the radial (r) and transversal (z) axes shown in the center of the figure. Subscripts: aerosol (a), sheath (sh), exhaust (exh), sample (sa), electrical (elec), centrifugal (cen).

Figure 4: Calculated transfer functions for the a) DMA (solid), b) AAC (dashed) and c) APM (dotted) in their native units of electrical mobility (Z_p), aerodynamic diameter (D_{ae}), and mass (m). d) all transfer functions converted to volume equivalent diameter (D_{ve}) for a spherical AS assuming a physical diameter of 250 nm and bulk density; see discussion in text.

Figure 5. a) Tandem DMA number density (N_{TDMA}) as a function of mobility diameter for AS particles with an aerodynamic diameter (D_{ae}) ≈ 250 nm. Particle net charge (q) is denoted as $q \rightarrow q'$ where q and q' correspond to the q in the first and second DMA, respectively. b) DMA-APM number density (N_{APM}) as a function of mass (m). The net charge +1 (green), +2 (cyan) and +3 (blue) on the particles is shown.

Figure 6. a) AAC-DMA number density (N_{SMPS}) as a function of mobility diameter for AS particles with aerodynamic diameter (D_{ae}) = 350 nm. b) AAC-APM number density (N_{APM}). The net charge +1 (green), +2 (cyan) and +3 (blue) on the particles is shown.

Figure 7. Comparison of three different measurements – AAC-DMA (circles, black), AAC-APM (squares, red), and DMA-APM (triangles, green) – of ammonium sulfate (AS) aerosol spanning D_{ae} from 150 nm to 550 nm. a) mobility diameter (D_m) determined from AAC-DMA measurement and AAC-APM calculation; b) D_m % deviation; c) particle mass (m); d) m % deviation; e) effective density (ρ_{eff}); f) ρ_{eff} % deviation; g) effective shape factor (χ_{eff}) and h) χ_{eff} % deviation.

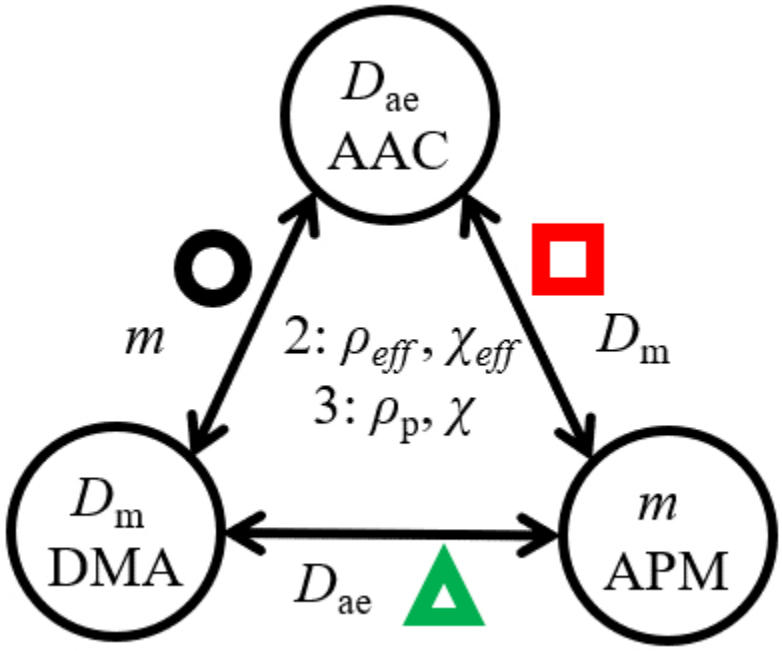

Figure 1. Schematic representation of the instruments and the corresponding measured values – mobility diameter (Dm), aerodynamic diameter (Dae) and particle mass (m) – the tandem measurement pairs (connected by lines) and the corresponding derived values. Pairwise combination allows for determination of effective density (ρeff) and effective dynamic shape factor (χeff). The combination of all three measurements allows for the quantitative determination of the dynamic shape factor (χ) and particle density (ρp). The circle (black), square (red) and triangle (green) are used throughout the manuscript to denote the corresponding measurement results.

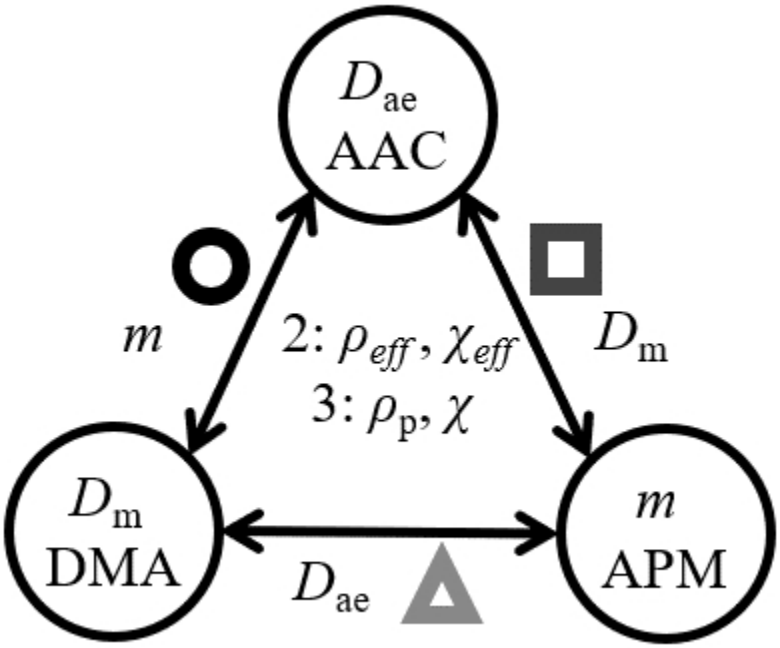

Figure 1. Schematic representation of the instruments and the corresponding measured values – mobility diameter (Dm), aerodynamic diameter (Dae) and particle mass (m) – the tandem measurement pairs (connected by lines) and the corresponding derived values. Pairwise combination allows for determination of effective density (ρeff) and effective dynamic shape factor (χeff). The combination of all three measurements allows for the quantitative determination of the dynamic shape factor (χ) and particle density (ρp). The circle (black), square (red) and triangle (green) are used throughout the manuscript to denote the corresponding measurement results.

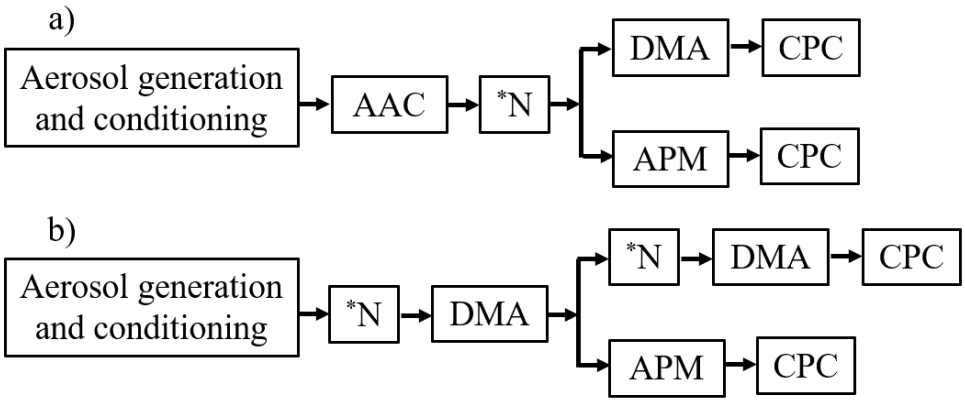

Figure 2. Block diagram of the two experimental setups (a and b) used in this study to achieve three configurations (AAC-DMA, AAC-APM, DMA-APM). *N corresponds to soft x-ray charge neutralizer.

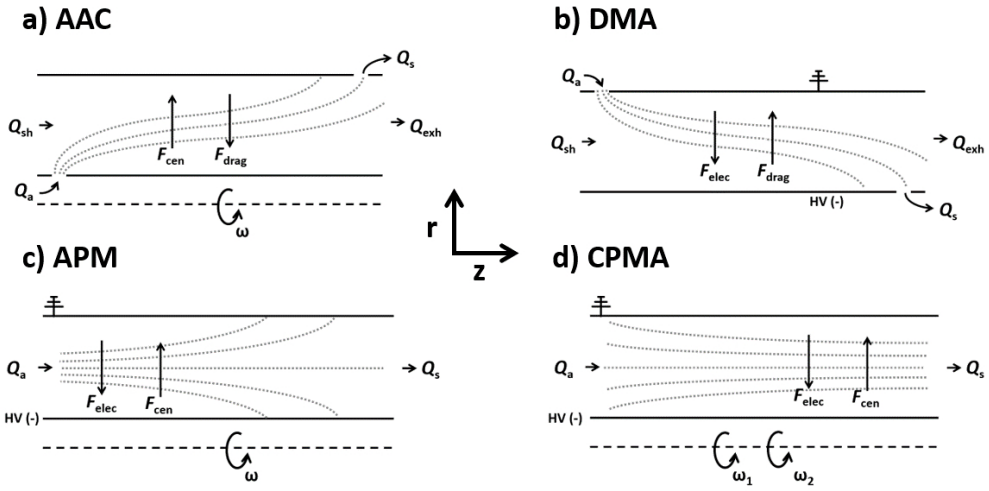

Figure 3. Forces (F), flows (Q), axes of rotation (ω) and particle trajectories (dotted grey lines) in the a) aerodynamic aerosol classifier (AAC), b) differential mobility analyzer (DMA), c) the aerosol particle mass analyzer (APM) and d) the centrifugal particle mass analyzer (CPMA). All figures are oriented with the radial (r) and transversal (z) axes shown in the center of the figure. Subscripts: aerosol (a), sheath (sh), exhaust (exh), sample (sa), electrical (elec), centrifugal (cen).

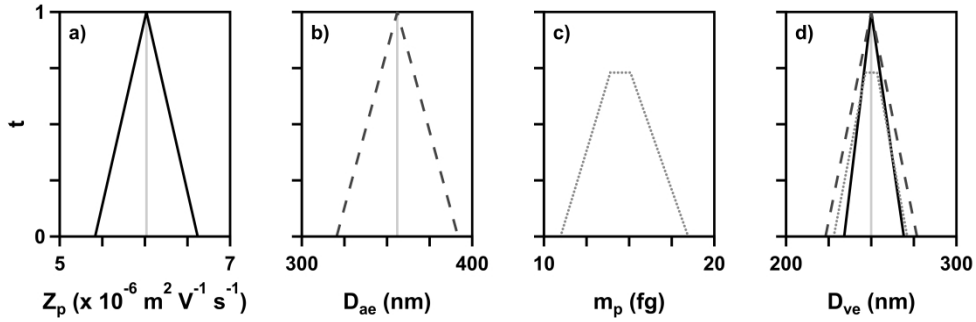

Figure 4: Calculated transfer functions for the a) DMA (solid), b) AAC (dashed) and c) APM (dotted) in their native units of electrical mobility (Zp), aerodynamic diameter (Dae), and mass (m). d) all transfer functions converted to volume equivalent diameter (Dve) for a spherical AS assuming a physical diameter of 250 nm and bulk density; see discussion in text.

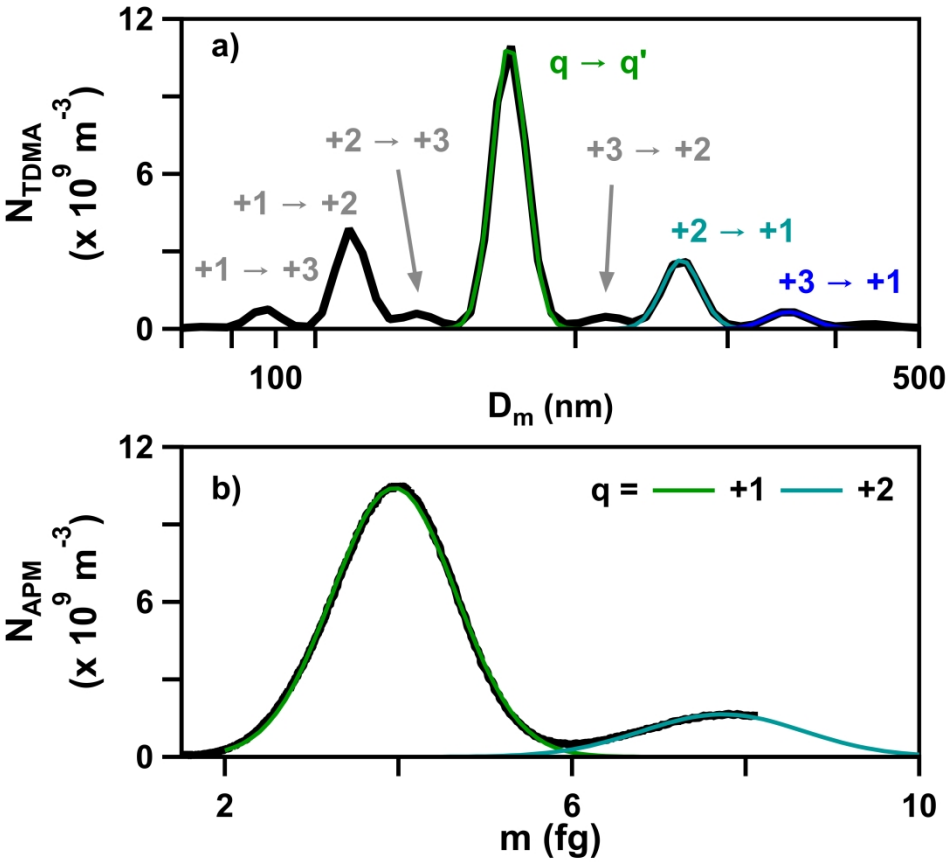

Figure 5. a) Tandem DMA number density (NTDMA) as a function of mobility diameter for AS particles with an aerodynamic diameter (Dae) ≈ 250 nm. Particle net charge (q) is denoted as q → q' where q and q' correspond to the q in the first and second DMA, respectively. b) DMA-APM number density (NAPM) as a function of mass (m). The net charge +1 (green), +2 (cyan) and +3 (blue) on the particles is shown.

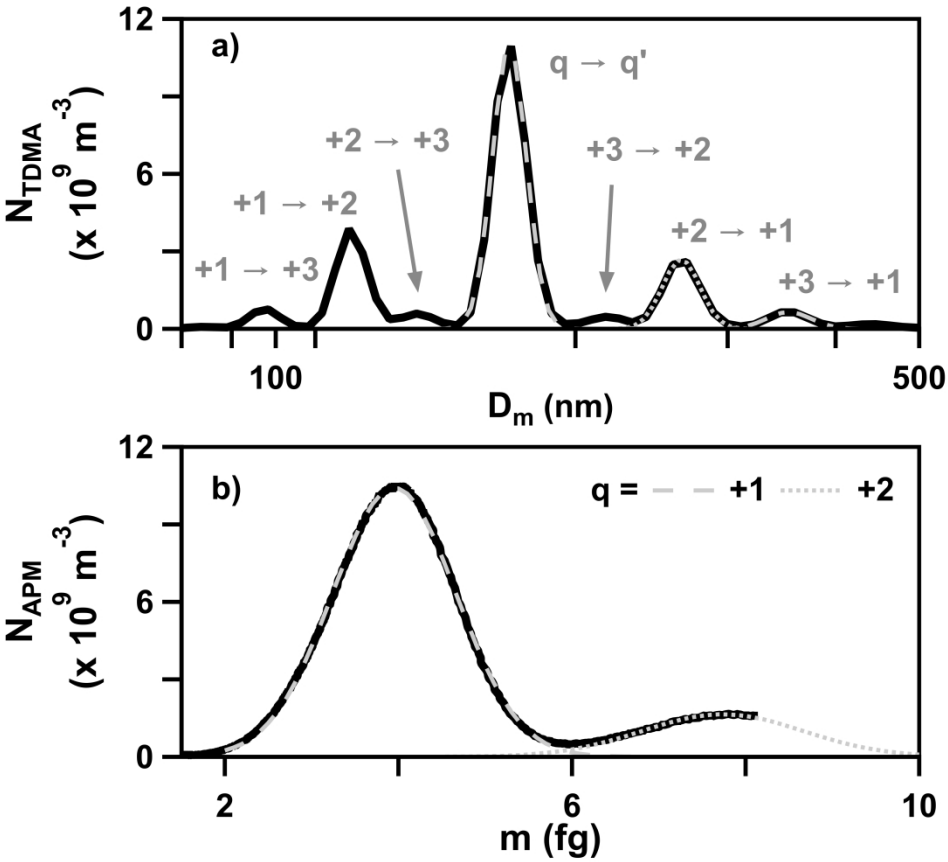

Figure 5. a) Tandem DMA number density (NTDMA) as a function of mobility diameter for AS particles with an aerodynamic diameter (Dae) ≈ 250 nm. Particle net charge (q) is denoted as q → q' where q and q' correspond to the q in the first and second DMA, respectively. b) DMA-APM number density (NAPM) as a function of mass (m). The net charge +1 (green), +2 (cyan) and +3 (blue) on the particles is shown.

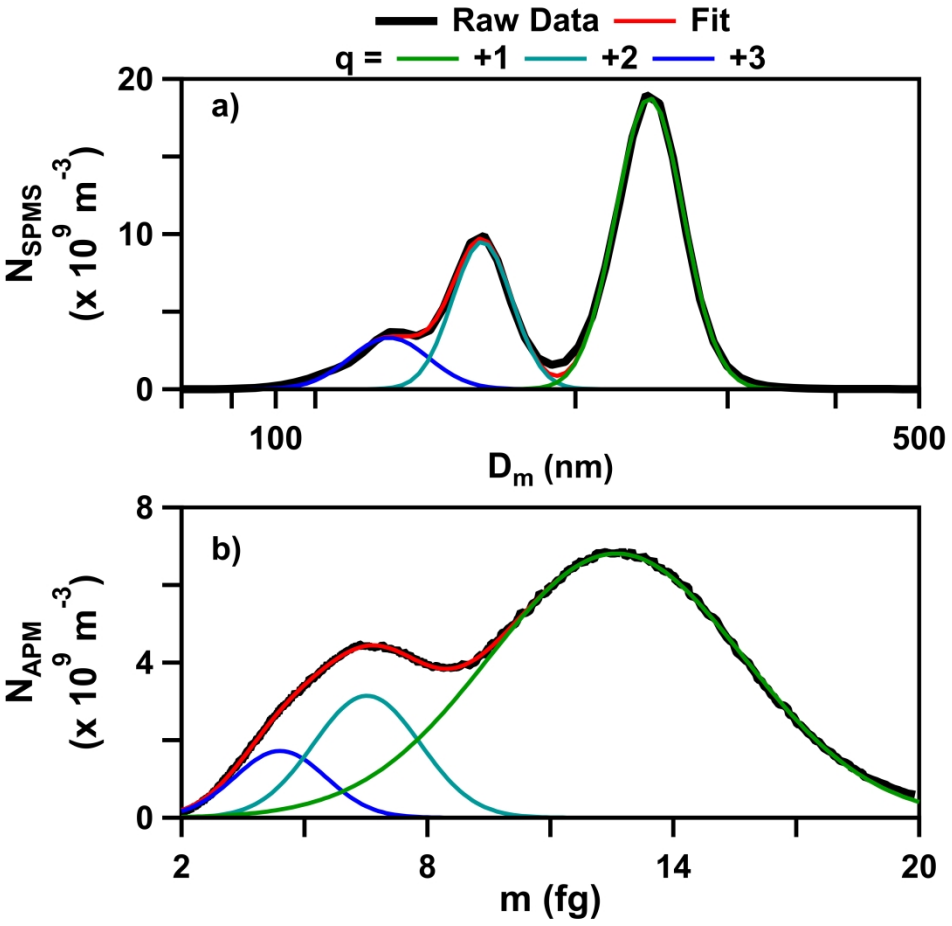

Figure 6. a) AAC-DMA number density (NSMPS) as a function of mobility diameter for AS particles with aerodynamic diameter (Dae) = 350 nm. b) AAC-APM number density (NAPM). The net charge +1 (green), +2 (cyan) and +3 (blue) on the particles is shown.

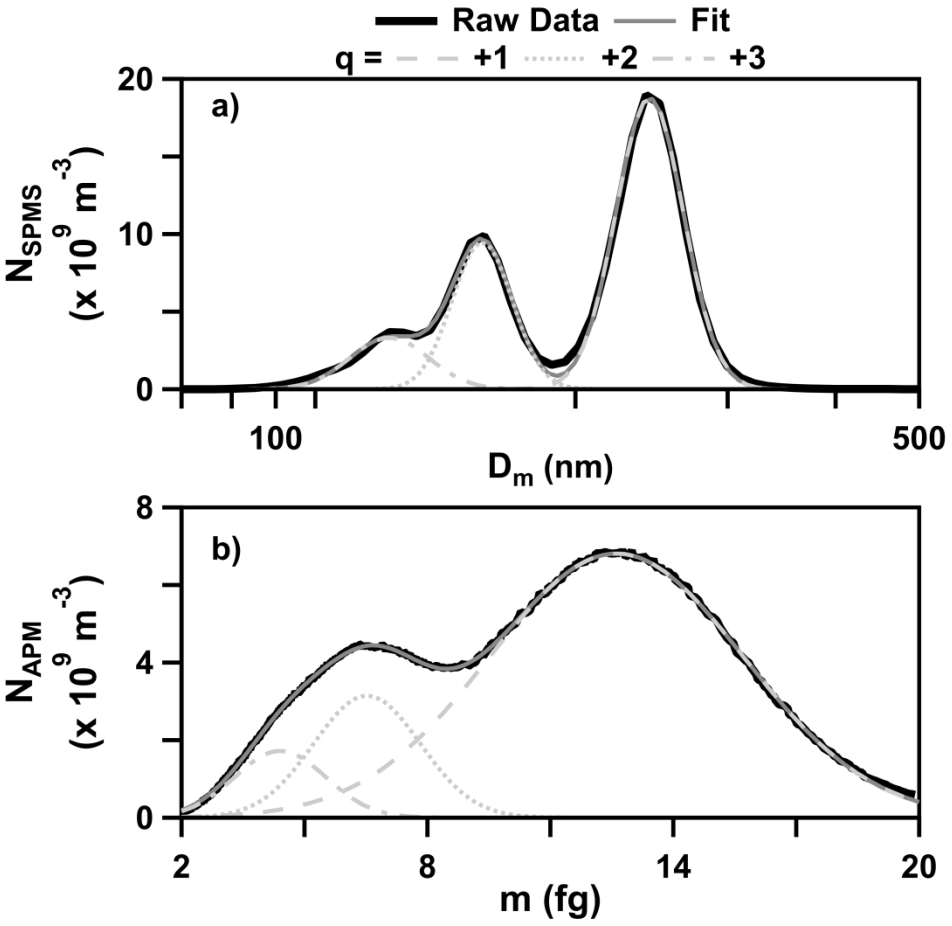

Figure 6. a) AAC-DMA number density (NSMPS) as a function of mobility diameter for AS particles with aerodynamic diameter (Dae) = 350 nm. b) AAC-APM number density (NAPM). The net charge +1 (green), +2 (cyan) and +3 (blue) on the particles is shown.

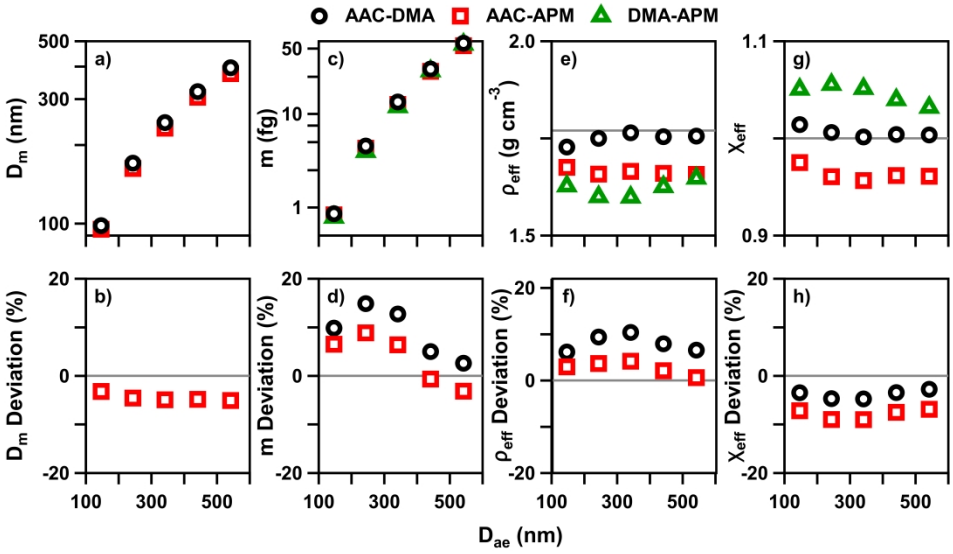

Figure 7. Comparison of three different measurements – AAC-DMA (circles, black), AAC-APM (squares, red), and DMA-APM (triangles, green) – of ammonium sulfate (AS) aerosol spanning Dae from 150 nm to 550 nm. a) mobility diameter (Dm) determined from AAC-DMA measurement and AAC-APM calculation; b) Dm % deviation; c) particle mass (m); d) m % deviation; e) effective density (ρeff); f) ρeff % deviation; g) effective shape factor (χeff) and h) χeff % deviation.

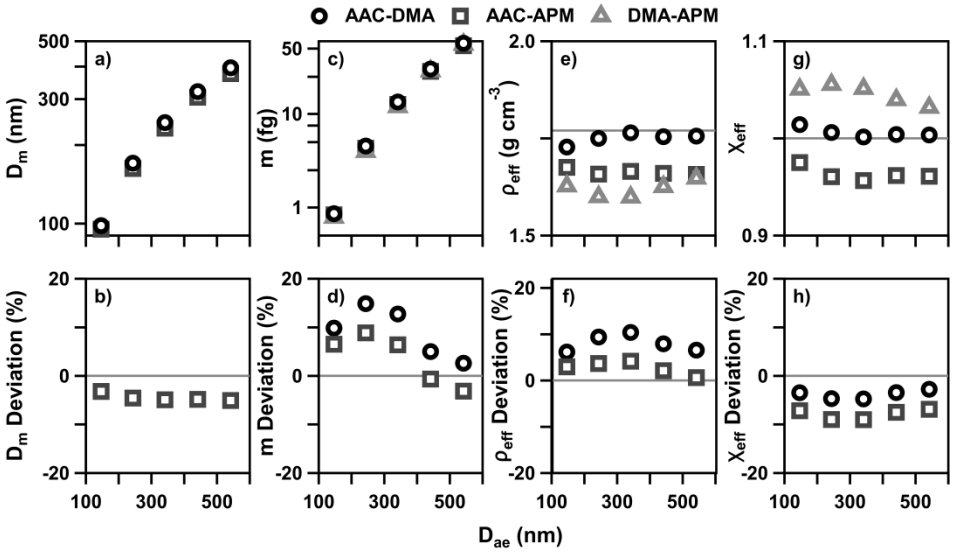

Figure 7. Comparison of three different measurements – AAC-DMA (circles, black), AAC-APM (squares, red), and DMA-APM (triangles, green) – of ammonium sulfate (AS) aerosol spanning Dae from 150 nm to 550 nm. a) mobility diameter (Dm) determined from AAC-DMA measurement and AAC-APM calculation; b) Dm % deviation; c) particle mass (m); d) m % deviation; e) effective density (ρeff); f) ρeff % deviation; g) effective shape factor (χeff) and h) χeff % deviation.

Table 1. Measured and calculated parameters for CB

Measured			Calculated					
τ (ns)	m_p (fg)	B (x 10^{10} m N^{-1} s^{-1})	χ	D_{ae} (nm)	D_m (nm)	ρ_{eff} (g cm^{-3})	D_{ve} (nm)	ρ_p (g cm^{-3})
149.5	1.82	7.949	1.036	145.3	156.6	0.902	152.9	0.971
224.4	4.29	4.750	1.100	186.5	217.8	0.793	204.5	0.959
314.6	7.87	3.578	1.117	231.5	264.2	0.816	244.3	1.031
417.9	13.71	2.705	1.127	276.4	322.4	0.781	295.1	1.018
538.6	21.97	2.229	1.100	329.0	372.1	0.814	346.5	1.009
665.8	32.48	1.853	1.106	372.0	428.5	0.788	395.4	1.004

Supporting Information for:

Comparison of three essential sub-micrometer aerosol measurements: mass, size and shape

Qi Yao[a], Akua Asa-Awuku[a,b], Christopher D. Zangmeister[c], James G. Radney[c]

[a] Department of Chemical and Biomolecular Engineering, University of Maryland, College Park, MD 20742 USA

[b] Department of Chemistry and Biochemistry, University of Maryland, College Park, MD 20742 USA

[c] Material Measurement Laboratory, National Institute of Standards and Technology, Gaithersburg, MD 20899 USA

Here, we explicitly calculated the associated Type B uncertainties (those not based upon a statistical quantity, e.g. a standard deviation, but rather scientific judgment of other relevant information) for the AAC-DMA, AAC-APM and DMA-APM measurements and provide representative values for AS with D_{ae} = 250 nm (D_m ≈ 170 nm). All data reported in the manuscript represents a single replicate consisting of either a single electrical mobility or mass distribution measured by scanning the DMA or APM for 5 min or 10 min, respectively, thus not allowing the Type A uncertainties (e.g. standard deviation) to be assessed. Uncertainties are shown in Table S1 with the relevant equations listed in sections S1 through S4.

Table S1: Representative Type B uncertainties by method for the measured D_{ae} = 250 nm (D_m = 167 nm) AS particles.

	AAC-DMA	AAC-APM	DMA-APM
$u(\tau)/\tau$	0.011*	0.011*	0.021
$u(D_{ae})/D_{ae}$	0.014	0.014	0.016
$u(D_m)/D_m$	0.010	0.038	0.010
$u(B)/B$	0.005*	0.024	0.005*
$u(m_p)/m_p$	0.021	0.012*	0.012*
$u(\rho_{eff})/\rho_{eff}$	0.032	0.11	0.032
$u(\chi)/\chi$	0.029	0.036	0.032

* denotes measured quantities

S1. AAC uncertainty.

As demonstrated by (Tavakoli and Olfert 2013; Tavakoli and Olfert 2014), the particle relaxation time (τ) can be related to the physical parameters of the AAC, see Eq 11. The corresponding uncertainty ($u(\tau)$) is

$$\left[\frac{u(\tau)}{\tau}\right]^2 = \left[\frac{u(Q_{sh})}{Q_{sh}}\right]^2 + 4\left[\frac{u(\omega)}{\omega}\right]^2 + 4\left[\frac{u(r)}{r}\right]^2 + \left[\frac{u(L)}{L}\right]^2 \quad \text{(S1)}$$

Following (Tavakoli and Olfert 2014) we assume $u(\omega)$, $u(r)$ and $u(L)$ are 5 rpm, 5 µm and 2 mm, respectively. Since AAC performance was evaluated pre- and post-measurement by the manufacturer, we assume $u(Q_{sh})$ = 0.01 L min^{-1} instead of the 0.1 L min^{-1} recommended in the previous publication.

For an AS particle with D_{ae} = 250 nm, an aerosol flow rate (Q_{aero}) of 0.55 L min^{-1} and an assumed D_{ae} resolution (R_{ae}) of 10, the corresponding sheath flow (Q_{sh}) and ω are 2.75 L min^{-1} and 2280 rpm, respectively.

S2. DMA uncertainty.

Prior to performing the measurements presented in this manuscript, the DMA columns were cleaned, and the electrostatic classifiers were calibrated using polystyrene nanospheres with nominal diameters spanning 102 nm to 702 nm; see Figure S1. The corresponding slopes were 1.0097 ± 0.0005 and 1.0046 ± 0.0005 and are comparable to previous calibrations performed by our lab (Radney and Zangmeister 2018).

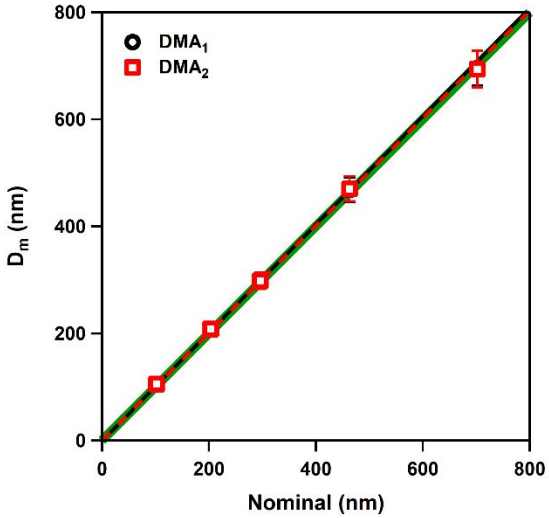

Figure S1: Measured D_m versus the nominal PSL diameter for both DMAs. Solid green line represents 1:1.

The DMA measures electrical mobility (Z_p) which can be related to the physical parameters of the classifier through Eq. 18. We derive $u(Z_p)$ from

$$x = \ln\left(r_2/r_1\right) \tag{S2}$$

$$u(x) = \frac{u\left(r_2/r_1\right)}{x} \tag{S3}$$

and

$$\left[\frac{u(Z_p)}{Z_p}\right]^2 = \left[\frac{u(Q_{sh})}{Q_{sh}}\right]^2 + \left[\frac{u(V)}{V}\right]^2 + \left[\frac{u(L)}{L}\right]^2 + \left[\frac{u(x)}{x}\right]^2 \tag{S4}$$

Q_{sh}:Q_{aero} was maintained at 10:1 for all measurements corresponding to 3.0 L min^{-1} and 5.5 L min^{-1} for the AAC-DMA and DMA-APM measurements, respectively. Following (Kinney et al. 1991) we assume $u(V)/V$ = 0.45 %, $u(L)/L$ = 0.5 %, $u(r_1)/r_1$ = 0.2 % and $u(r_2)/r_2$ = 0.3 % which gives $u(Z_p)/Z_p \approx$ 0.50 %. This is less than the calibration accuracy of ≈ 1 % ($u(D_m)/D_m$), but the calibration also includes effects from μ (1.2 %) (Tavakoli and Olfert 2014) and C_c (2.1 %) (Allen and Raabe 1985). It follows from Eq. 16 that the uncertainty in $B \approx$ 0.50 %

$$\left[\frac{u(B)}{B}\right]^2 = \left[\frac{u(Z_p)}{Z_p}\right]^2 + \left[\frac{u(e)}{e}\right]^2 \quad \text{(S5)}$$

S3. APM Uncertainty.

For the APM, the measured mass can be related to the physical properties of the classifier through Eq. 20 and we derive $u(m)/m$ is

$$\left[\frac{u(m)}{m}\right]^2 = \left[\frac{u(V)}{V}\right]^2 + 4\left[\frac{u(r)}{r}\right]^2 + 4\left[\frac{u(\omega)}{\omega}\right]^2 + \left[\frac{u(x)}{x}\right]^2 \quad \text{(S6)}$$

and L = 100 mm. Assuming a classification parameter (λ_c) of 0.32 (Ehara, Hagwood, and Coakley 1996) and an AS particle with D_m = 167 nm and m_p = 3.9 fg (Figure 3c) this translates to ω = 4115 rpm and V = 111 V. Similar to the AAC, we assume $u(\omega)$ is 5 rpm and u(r_1) = u(r2) = 5 µm.

S4. Uncertainty in derived parameters

For the AAC-DMA, τ and B are the measurands and m is the derived parameter. Following Eq. 35,

$$\left[\frac{u(m)}{m}\right]^2 = \left[\frac{u(\tau)}{\tau}\right]^2 + \left[\frac{u(B)}{B}\right]^2 + \left[\frac{u(\chi)}{\chi}\right]^2 \quad \text{(S7)}$$

and the ρ_{eff} (Eq. 22) uncertainty is

$$\left[\frac{u(\rho_{eff})}{\rho_{eff}}\right]^2 = \left[\frac{u(m)}{m}\right]^2 + 9\left[\frac{u(D_m)}{D_m}\right]^2 \quad \text{(S8)}$$

For the AAC-APM, τ and m are the measurands and B is the derived parameter. Thus, the uncertainty in D_m is

$$\left[\frac{u(D_m)}{D_m}\right]^2 = \left[\frac{u(B)}{B}\right]^2 + \frac{1}{4}\left[\frac{u(\chi)}{\chi}\right]^2 + \left[\frac{u(\mu)}{\mu}\right]^2 + \left[\frac{u(C_c(D_m))}{C_c(D_m)}\right]^2 \quad \text{(S9)}$$

For the DMA-APM, B and m_p are the measurands allowing for τ to be calculated from Eq. 35. It follows that D_{ae} can be calculated from Eq. 14 and the uncertainty is

$$\left[\frac{u(D_{ae})}{D_{ae}}\right]^2 = \frac{1}{4}\left[\frac{u(\tau)}{\tau}\right]^2 + \frac{1}{4}\left[\frac{u(\chi)}{\chi}\right]^2 + \frac{1}{4}\left[\frac{u(\mu)}{\mu}\right]^2 + \frac{1}{4}\left[\frac{u(C_c(D_{ae}))}{C_c(D_{ae})}\right]^2 \quad \text{(S10)}$$

For all derived parameters, $u(\chi)/\chi$ = 1.7 % was included in the determination of the derived parameter as outlined in Section 4.2. Data harmonization. This uncertainty was determined from the carbon black measurements utilizing the triplet of instrumentation in Section 4.3. When χ is not included but instead derived from measurements, the uncertainty u(χ)/χ takes different forms. For the AAC,

$$\left[\frac{u(\chi)}{\chi}\right]^2 = \frac{4}{9}\left[\frac{u(D_{\mathrm{m}})}{D_{\mathrm{m}}}\right]^2 + \frac{4}{9}\left[\frac{u(D_{\mathrm{ae}})}{D_{\mathrm{ae}}}\right]^2 + \frac{14}{9}\left[\frac{u(C_c)}{C_{\mathrm{c}}}\right]^2 + \frac{1}{9}\left[\frac{u(\rho_{\mathrm{p}})}{\rho_{\mathrm{p}}}\right]^2 \quad \text{(S11)}$$

We assume a $u(\rho_{\mathrm{p}}) = 0.01$, so for AS, $u(\rho_{\mathrm{p}})/\rho_{\mathrm{p}} = 0.006$. For DMA-APM measurements,

$$\left[\frac{u(\chi)}{\chi}\right]^2 = \left[\frac{u(D_{\mathrm{m}})}{D_{\mathrm{m}}}\right]^2 + 2\left[\frac{u(C_c)}{C_{\mathrm{c}}}\right]^2 + \left[\frac{u(D_{\mathrm{ve}})}{D_{\mathrm{ve}}}\right]^2 \quad \text{(S12)}$$

S5. AS Raw data

Table S2: AS raw data for experiments shown in Figure 2a.

AAC[a]	DMA[b]	APM[b]
τ (ns)	D_{m} (nm)	m (fg)
150	98.3	0.832
315.1	170.5	4.30
538.9	244.0	12.7
824.4	320.4	28.6
1171.7	395.8	53.8

[a] Instrumental setpoint
[b] Determined by fitting scanned distribution.

Table S3: AS raw data for experiments shown in Figure 2b.

DMA[a]	APM[b]
D_{m} (nm)	m (fg)
97.2	0.782
167.7	3.95
242.3	11.91
323.4	28.78
400.9	55.57

[a] Instrumental setpoint
[b] Determined by fitting scanned distribution.

References

Allen, M. D., and Raabe. O. G. 1985. Slip Correction Measurements of Spherical Solid Aerosol Particles in an Improved Millikan Apparatus. *Aerosol Science and Technology* 4 (3): 269–86. https://doi.org/10.1080/02786828508959055.

Ehara, K., Hagwood, C., and Coakley, K. J. 1996. Novel Method to Classify Aerosol Particles According to Their Mass-to-Charge Ratio - Aerosol Particle Mass Analyser. *Journal of Aerosol Science* 27 (2): 217–34. https://doi.org/10.1016/0021-8502(95)00562-5.

Kinney, P.D., D.Y.H. Pui, G.W. Mulholland, and N.P. Bryner. 1991. Use of the Electrostatic Classification Method to Size 0.1 Micrometer SRM Particles - A Feasibility Study. *Journal of Research of the National Institute of Standards and Technology* 96 (2): 147. https://doi.org/10.6028/jres.096.006.

Radney, J. G., You, R., Ma, X. F., Conny, J. M., Zachariah, M. R., Hodges, J. T., and Zangmeister, C. D. 2014. "Dependence of Soot Optical Properties on Particle Morphology: Measurements and Model Comparisons." *Environmental Science & Technology* 48 (6): 3169–76. https://doi.org/10.1021/es4041804.

Radney, J. G., and Zangmeister, C. D. 2018. Comparing Aerosol Refractive Indices Retrieved from Full Distribution and Size- and Mass-Selected Measurements. *Journal of Quantitative Spectroscopy and Radiative Transfer* 220 (November): 52–66. https://doi.org/10.1016/j.jqsrt.2018.08.021.

Tavakoli, F., and Olfert, J. S. 2013. An Instrument for the Classification of Aerosols by Particle Relaxation Time: Theoretical Models of the Aerodynamic Aerosol Classifier. *Aerosol Science and Technology* 47 (8): 916–26. https://doi.org/10.1080/02786826.2013.802761.

Tavakoli, F., and Olfert, J. S. 2014. Determination of Particle Mass, Effective Density, Mass–Mobility Exponent, and Dynamic Shape Factor Using an Aerodynamic Aerosol Classifier and a Differential Mobility Analyzer in Tandem. *Journal of Aerosol Science* 75 (September): 35–42. https://doi.org/10.1016/j.jaerosci.2014.04.010.